A&A 668, A22 (2022)
https://doi.org/10.1051/0004-6361/202244222

Astronomy & Astrophysics

Understanding dust production and mass loss in the AGB phase using post-AGB stars in the Magellanic Clouds

S. Tosi[1,2], F. Dell'Agli[2], D. Kamath[3,4], P. Ventura[2,5], H. Van Winckel[6], and E. Marini[2]

[1] Dipartimento di Matematica e Fisica, Universitá degli Studi Roma Tre, via della Vasca Navale 84, 00100, Roma, Italy
e-mail: silvia.tosi@uniroma3.it
[2] INAF, Observatory of Rome, Via Frascati 33, 00077 Monte Porzio Catone, RM, Italy
[3] School of Mathematical and Physical Sciences, Macquarie University, Sydney, NSW, Australia
[4] Astronomy, Astrophysics and Astrophotonics Research Centre, Macquarie University, Sydney, NSW, Australia
[5] Istituto Nazionale di Fisica Nucleare, section of Perugia, Via A. Pascoli snc, 06123 Perugia, Italy
[6] Institute of Astronomy, K.U. Leuven, Celestijnenlaan 200D bus 2401, 3001 Leuven, Belgium

Received 8 June 2022 / Accepted 15 August 2022

ABSTRACT

Context. The asymptotic giant branch (AGB) phase of evolution in low- and intermediate-mass stars is governed by poorly understood physical mechanisms, such as convection, mixing, dust production and mass loss, which play a crucial role in determining the internal structure and the evolution of these stars. The spectra of post-asymptotic giant branch (post-AGB) stars hold critical chemical fingerprints that serve as exquisite tracers of the evolution, nucleosynthesis, and dust production during the AGB phase.
Aims. We aim to understand the variation in the surface chemistry that occurs during the AGB phase by analysing results from observations of single post-AGB stars in the Magellanic Clouds. We also aim to reconstruct dust-formation processes, which are active in the circumstellar envelope of AGB stars, occurring towards the end of the AGB phase and during the subsequent course of evolution when contraction to the post-AGB has begun.
Methods. We study likely single post-AGB sources in the Magellanic Clouds that exhibit a double-peaked (shell-type) spectral energy distribution (SED). We interpret their SED by comparing with results from radiative transfer calculations to derive the luminosity and the dust content of the individual sources. Additionally, we compare the observationally derived stellar parameters and the photospheric chemical abundances of the target sample with results from stellar evolution modelling of AGB and post-AGB stars. This allows for the characterization of the individual sources in terms of the initial mass and formation epoch of the progenitors. The theoretically derived dust mineralogy and optical depth is used to assess when dust formation ceases and to determine the propagation velocity of the dust-gas system during post-AGB evolution.
Results. We find that amongst our target sample of 13 likely single post-AGB stars with shell-type SED, eight objects are carbon stars descending from ∼1−2.5 $M_{\odot}$ progenitors. Five of the 13 objects are of lower mass, descending from $M < 1\,M_{\odot}$ stars. Based on the dust mineralogy, we find that these five stars are surrounded by silicate dust, and thus failed to become carbon stars. The dust optical depth and the luminosity of the stars are correlated, owing to the faster evolutionary timescale of brighter stars, which makes the dusty layer closer to the central object. From our detailed analysis of the SEDs, we deduce that the dust currently observed around post-AGB stars was released after the onset of the central star contraction and an increase in the effective temperature to ∼3500−4000 K.

Key words. stars: AGB and post-AGB – stars: abundances – stars: evolution – stars: winds, outflows

1. Introduction

After the core helium burning phase, single stars with an initial mass below ∼8 $M_{\odot}$ (i.e. low- and intermediate-mass stars) evolve through the asymptotic giant branch (AGB). When the mass of the envelope drops below a few hundredths of solar mass, the external regions of the star contract, and thus post-AGB evolution begins (Iben & Renzini 1983). During this phase the stars evolve at constant luminosity and readjust into a configuration that becomes increasingly compact over time, with the effective temperature increasing from ∼3000 K to ∼30 000 K. The post-AGB phase is then followed by planetary nebula evolution, before the white dwarf cooling phase (Iben & Renzini 1983).

The AGB phase is characterized by the occurrence of two physical phenomena that are able to alter the surface chemistry of these stars: third dredge-up (TDU, Iben 1974) and hot bottom burning (HBB, Sackmann & Boothroyd 1992). These mechanisms are still not fully understood from first principles and the information derived from the analysis and the characterization of post-AGB stars proves an exceptionally valuable tool for this purpose. The main reason for this is twofold: their chemical composition represents the final outcome of AGB evolution and the associated internal enrichment processes. Another reason is that the surface abundances of post-AGB stars can be determined accurately, given that their spectra are dominated by atomic transitions.

Furthermore, given the peculiar morphology of the spectral energy distribution (SED) of post-AGB stars (Woods et al. 2011), the study of the infrared (IR) excess allows a reliable determination of the dust properties, in terms of mineralogy, optical thickness, and the current distance from the central star; this kind of analysis provides important information on the dust-formation process in the wind of AGB stars during the final evolutionary phases, and more generally on the efficiency of dust formation in the circumstellar envelope of evolved giants. This step is of paramount importance in order to evaluate the role that

AGB stars play as dust manufacturers; indeed, it was shown that a few stars evolving through the late-AGB phases are responsible for most of the current dust-formation rates in the dwarf irregular galaxies such as IC1613 (Dell'Agli et al. 2016), IC10 (Dell'Agli et al. 2018), Sextans A (Dell'Agli et al. 2019).

In the present work, we use results from observations of post-AGB stars to characterize the individual sources in terms of mass and age of the progenitor stars. This step offers the possibility of testing the current AGB evolution theories, particularly when the surface chemistry of the stars is known from the observations, and can be compared with theoretical predictions. Furthermore, the analysis of the IR excess is used to shed new light on the dust-formation process during the very late-AGB phases and possibly after the beginning of the contraction to the post-AGB phase. This investigation can give information on the timescale of the AGB to post-AGB transition, and to investigate the dynamics of the wind moving away from the star after dust production ceases.

This study benefits from the rich dataset of optically visible post-AGB stars observed in the Magellanic Clouds (Kamath et al. 2014, 2015, hereafter K14 and K15). For the single stars in these samples, the availability of the optical and IR data allowed the reconstruction of the SED and the determination of the IR excess, which proved essential for an estimate of the luminosity, and for the determination of the mineralogy and amount of dust in the surroundings of the star.

The stars are interpreted and characterized in light of updated AGB evolutionary sequences, which are extended on purpose until and past the post-AGB phase. These tracks also include the description of the dust-formation process, following the schematization proposed by the Heidelberg group (Ferrarotti & Gail 2006), in the wake of previous studies on dust production by evolved stars proposed by our team (Ventura et al. 2012, 2014). These studies have been used to interpret the evolved stellar populations of the Magellanic Clouds (Dell'Agli et al. 2014a,b, 2015a,b) and of Local Group galaxies (Dell'Agli et al. 2016, 2018, 2019), and to explore the potentialities in this field offered by the recent launch of the James Webb Space Telescope (JWST) (Marini et al. 2020, 2021).

The paper is structured as follows. Section 2 includes the description of the codes used to model the evolution of the star and the dust-formation process during the AGB and the early post-AGB phases. This section also describes the methodology followed to interpret the optical and IR observations of the selected sources, to derive the luminosities and the properties of the dust in their surroundings. The results of the SED fitting analysis are given in Sect. 3, and in Sect. 4 we characterize the sources individually, in order to find out the mass and age of the progenitors. Section 5 presents the results for the mass loss suffered by the stars during the late-AGB phases, which are in agreement with the expectations from stellar evolution modelling. In Sect. 6 we discuss the properties of the wind and of the physics of the AGB to post-AGB transition, based on the results obtained in the previous sections. Finally, the conclusions are given in Sect. 7.

2. Numerical, chemical, and physical input

The characterization of the stars considered in the present study is based on results from stellar evolution and dust-formation modelling, which are used in synergy with the SED fitting analysis, applied to all the sources investigated. In the following paragraphs we describe the most relevant physical ingredients of the codes used to model the evolution of the star, to describe the dust-formation process in the outflow, and to build synthetic SEDs, which are compared with the observational dataset available.

2.1. AGB and post-AGB modelling

The evolutionary sequences were calculated by means of the stellar evolution code ATON, extensively described in Ventura et al. (1998). The code performs a full integration of the stellar structure equations, from the centre of the star to the photosphere. The temperature gradient within regions unstable to convection is found via the Full Spectrum of Turbulence model (Canuto & Mazzitelli 1991). The formal borders of the convective regions are found via the classic Schwartzschild criterion; however, convective eddies are allowed to overshoot into radiatively stable regions, by imposing an exponential decay of velocities beyond the formal border. This approach, which is consistent with results from numerical simulations (Freytag et al. 1996), was also used for example, by Herwig (2000). In the convective regions (including the overshoot zones), nuclear burning and mixing of chemicals are self-consistently coupled by means of the diffusive approach proposed by Cloutman & Eoll (1976). Mass loss during the oxygen-rich phases is described using the formulation by Blöcker (1995); for carbon stars we use the treament proposed by the Berlin group (Wachter et al. 2002, 2008).

The metallicities of the stars considered here span the $-1 \leq$ [Fe/H] ≤ -0.4 range. We divided the sources in two groups, according to their metallicity, and we used the $Z = 2 \times 10^{-3}$ and $Z = 4 \times 10^{-3}$ evolutionary tracks that we calculated for the study by Kamath et al. (2021) to study the stars of lower and higher metallicity, respectively. To investigate the highest-luminosity objects, we extended the set of models by Kamath et al. (2021) to include $2\,M_{\odot}$ and $2.5\,M_{\odot}$ evolutionary sequences of metallicity $Z = 2 \times 10^{-3}$, which were calculated on purpose for the present work. Furthermore, the study of the faintest stars required the calculation of $0.65\,M_{\odot}$ and $0.7\,M_{\odot}$ models of the same metallicity.

2.2. The description of dust formation in the wind of evolved stars

For some selected points along the evolutionary tracks, we used the physical parameters of the stars, namely mass, luminosity, effective temperature, mass-loss rate, and surface chemical composition, to determine the dust-production rate. To this end, we relied on the schematization proposed by the Heidelberg group (Ferrarotti & Gail 2006), according to which the dust forms in a stationary wind, expanding radially from the photosphere of the star.

The wind velocity v is found via the equation of momentum conservation, which is

$$\frac{\mathrm{d}v}{\mathrm{d}r} = -\frac{GM_*}{r^2}(1-\Gamma), \tag{1}$$

where r is the radial distance from the centre of the star, M_* is the (current) mass of the star, and $\Gamma = kL_*/4\pi cGM_*$. In the expression for Γ, which represents the relative weight of the effects of radiation pressure and gravity, L_* is the luminosity of the star, whereas k is the extinction coefficient, which reflects the scattering and absorption processes of the photons released from the stellar photosphere by dust particles. Therefore, the growth of dust grains and the dynamics of the wind are self-consistently coupled, as the calculation of k requires the determination of the size of the dust particles of the different species formed.

The description of the wind is completed by the radial profiles of the density, which for mass conservation reasons is expressed by the equation

$$\rho = \frac{\dot{M}}{4\pi r^2 v}, \tag{2}$$

where $\dot{M}$ is the mass-loss rate, whereas v is the wind velocity at distance r from the centre of the star.

The relevant equations and the details of the numerical treatment are extensively described, for example, in Ventura et al. (2012, 2014). The knowledge of the radial stratification of the thermodynamic variables and of the grain sizes of the various dust species allows the calculation of the optical depth, which is found via the following expression:

$$\tau_{10} = \pi \int_{r_{\rm in}}^{r_{\rm out}} n_{\rm d} Q_{10} a^3 {\rm d}r, \tag{3}$$

where $n_{\rm d}$ and a are the number density and the size of the dust grains, Q_{10} is the extinction coefficient at 10 μm, and $r_{\rm in}$ and $r_{\rm out}$ are the distances of the inner and outer borders of the region of the circumstellar envelope populated by dust particles. The overall optical depth must be calculated by summing all the contributions from the individual dust species, the largest contribution being given by those with the highest extinction coefficients (i.e. solid carbon or silicate dust).

2.3. SED Fitting

To build synthetic SED for the comparison with the observational data points, we used the radiation transfer code DUSTY, described in Nenkova et al. (1999). The code calculates the SED emerging from the star by accounting for the reprocessing of the radiation released from the photosphere by a dusty region that is isotropically distributed around the source.

To describe the input radiation entering the dusty layer, we used the Kurucz-Castelli atmosphere models (Castelli & Kurucz 2003), available for a wide range of metallicities and effective temperatures. The effects of dust reprocessing are taken into account by specifying the optical depth τ_{10} (see Eq. (3) above for the definition) and the dust temperature in the inner border of the dusty region, $T_{\rm d}$.

Regarding the dust mineralogy, we considered the possibility that the dust is either composed entirely of silicates, or it is pure carbon dust. In the latter case, for the higher-metallicity sources, we further explored the possibility that some fraction of silicon carbide is present.

The size of the dust particles was chosen on the basis of the results from dust-formation modelling, described in Sect. 2.2. One of the outcomes of this modelling is the asymptotic size of the individual species attained by the dust grains, which is used as input for the dusty code. Typically, we adopt 0.12 μm for solid carbon, 0.07 μm for SiC, and 0.08 μm for silicates.

The optical constants required as input by DUSTY and considered in the present analysis are the following: Ossenkopf et al. (1992) for silicates; Zubko et al. (1996) for amorphous carbon; and Pegourie (1988) for silicon carbide. We considered the possibility that in the low-temperature domain, the silicates assume a crystalline form, in which case we used the optical constants by Jaeger et al. (1994).

3. The analysis of SEDs of the target sample of post-AGB stars

K14 and K15 assembled results from optical and IR photometry of evolved stars in the Magellanic Clouds, and reconstructed the shape of the SED of the different sources over an extended spectral region. In this work we focus on 13 single stars that were classified as shell-type post-AGB stars by K14 and K15. This choice allows us to use the code DUSTY, described in Sect. 2.3, in an attempt to provide an interpretation of the data of the different sources.

Our approach is to confront results from synthetic SED modelling with the photometric dataset, to derive the most relevant quantities related to the individual stars, namely the luminosity, dust mineralogy, optical depth, and dust temperature of the internal border of the dusty region. We could compare the synthetic SED with the IR spectrum (Volk et al. 2011) for only one of the sources considered, namely J004441.03.

To this end, we start from the effective temperatures and metallicities reported in K14 and K15, or, when available, from high-resolution spectroscopy analysis. This information is required to calculate the input spectrum released from the photosphere of the star, and entering the dusty zone. We adjust the input parameters required to produce the synthetic SED, until a satisfactory agreement with the observations is reached. This procedure leads to the derivation of the stellar luminosity and of the dust quantities, according to the following steps.

We first derive the dust mineralogy, based on the fact that the shape of the SED of carbon stars differs significantly from that of stars surrounded by silicates in the 20−30 μm spectral region; indeed the presence of silicates causes a strongly negative slope of the flux with λ at wavelengths above ∼20 μm, whereas in the case of carbon stars, the SED is still decreasing in the same spectral region, but it is significantly flatter.

The second step consists in the determination of the optical depth of the dust surrounding the individual sources, which can be accurately derived, because the dust layer is sufficiently far from the surface of the star so that the IR excess in the 8−30 μm spectral region is indeed dependent on τ_{10} only.

The peculiar morphology of the SED of post-AGB stars allows the determination of the dust temperature $T_{\rm d}$ of the internal border of the dust zone, which is extremely sensitive to the depth and the location of the minimum in the SED, usually found in the 3−6 μm spectral region.

To derive the values of the interstellar reddening we rely on the morphology of the SED in the optical part of the spectrum; we find consistency with the results published in K14 and K15. Finally, the luminosity of the star can be estimated by shifting the synthetic SED until matching the observed SED profile in the near-IR region.

Once the mineralogy of the dust is determined, the dust temperature can be derived with an accuracy of the order of 10−20 K. In the cases where WISE, IRAC, and MIPS photometry are available, the optical depth can be fixed with a 10−15% precision. Finally, the luminosity of the stars is established mostly from the near-IR part of the spectrum with an uncertainty within 10%.

Figures 1 and 2 show the analysis performed for each of the sources considered, divided according to whether they are interpreted as surrounded by carbon dust or silicates, respectively. We note that the error bars of the photometric data of the post-AGB stars in the Small Magellanic Cloud (SMC) and the Large Magellanic Cloud (LMC). In the cases where multi-epoch observations for the same band are available, we show all the results in

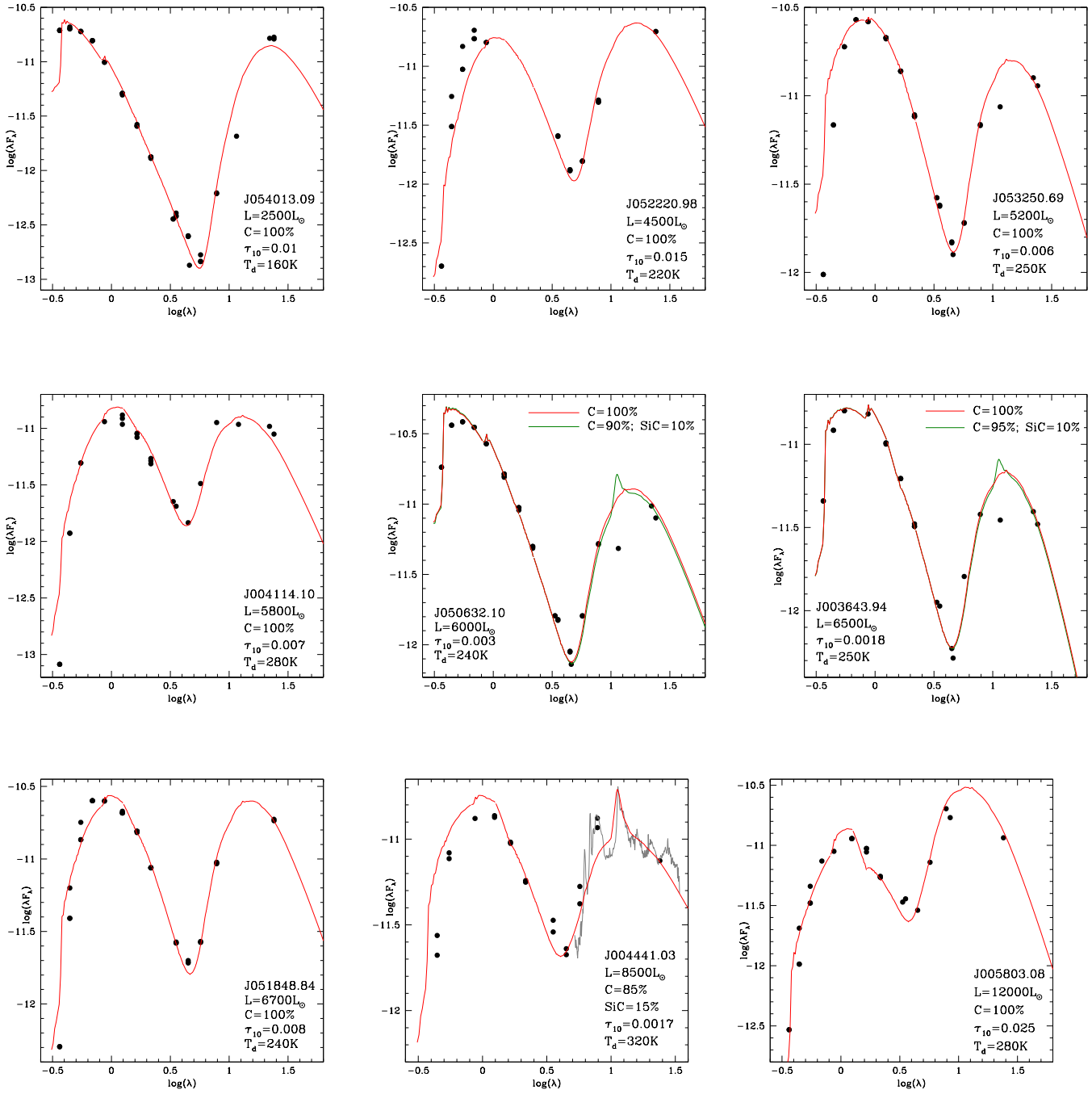

Fig. 1. Optical and IR data (black points) of SMC and LMC sources classified as post-AGB stars with a shell-like structure by K14 and K15, which we interpret as surrounded by carbonaceous dust in the present investigation. The grey line in the *middle panel* of the bottom line shows the IR spectroscopy results from Volk et al. (2011). The red lines indicate the best-fit model obtained by the DUSTY code. The derived stellar and dust parameters for each source are shown in the different panels.

a vertical sequence, in conjunction with the central wavelength of the corresponding filter.

Table 1 reports the metallicities, the effective temperatures, and the quantities derived from SED fitting, namely the luminosities and the dust properties (i.e. the mineralogy, the optical depth, the dust temperature, and the distance from the centre of the star of the inner border of the dust layer. The last column gives the estimated mass of the progenitors at the beginning of the AGB phase (see next section).

We find that the dust in the surroundings of the stars that we classify as oxygen-rich sources is composed of a mixture of amorphous and crystalline silicates, with the latter component accounting for ∼50% of the total dust. The presence of a significant fraction of dust in the crystalline form is required to reproduce the strongly negative slope of the SED in the $\lambda > 20\,\mu$m spectral region, as determined by the combination of the WISE4 and MIPS data. Use of a pure amorphous dust in the SED fitting procedure does not allow the shape of the SED to be reproduced, independently of the optical constants adopted.

We note that this conclusion relies on the assumptions upon which the DUSTY code is based, namely that the dusty zone

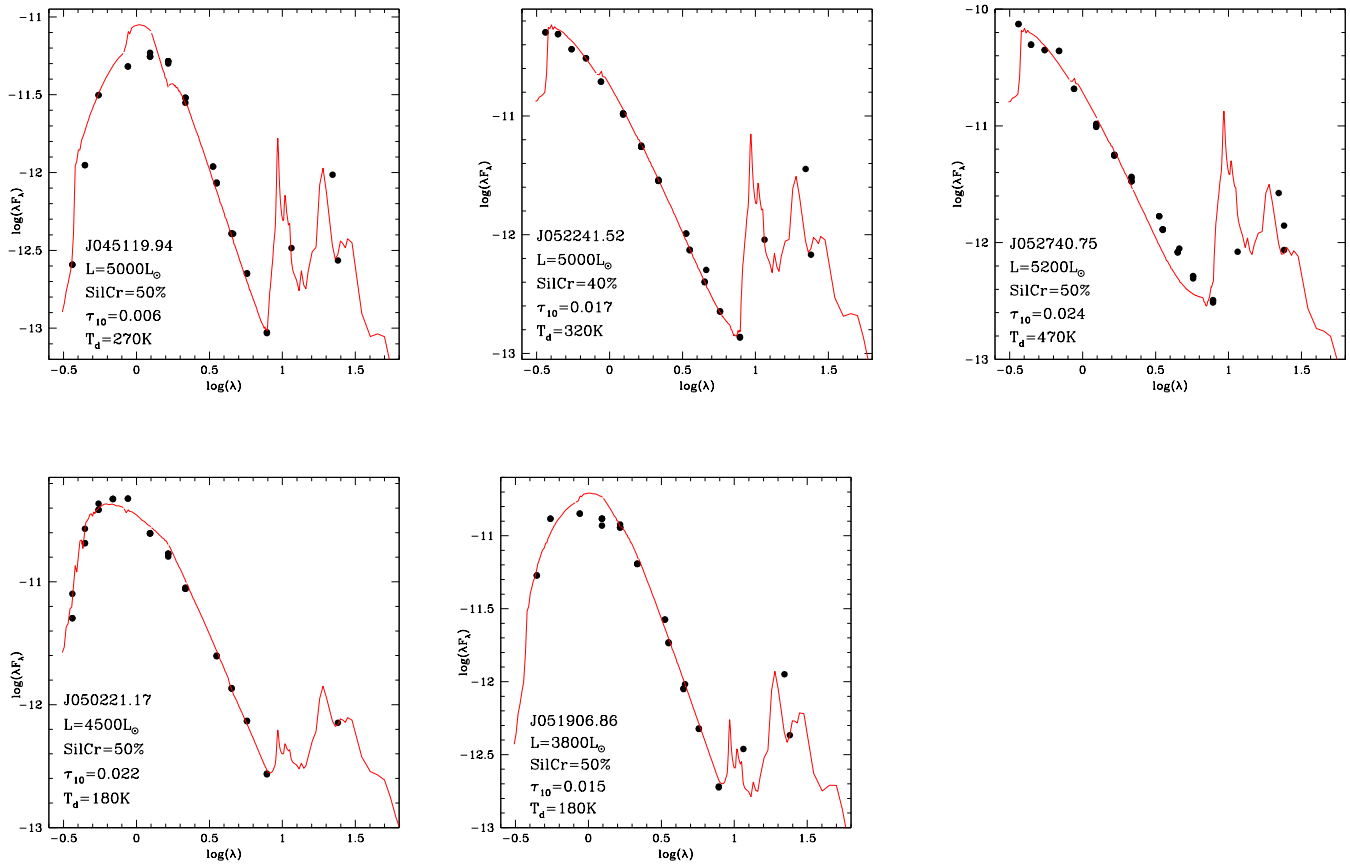

Fig. 2. Same as for Fig. 1, but reporting the sources that we interpret as surrounded by silicate dust. The symbols used are the same as in Fig. 1. The fraction of silicate dust in the crystalline form is given in each panel.

Table 1. Physical and dust properties of the LMC and SMC sources classified as shell-type post AGB stars by K14 and K15.

ID	[Fe/H]	$T_{\rm eff}$[K]	$L/L_\odot$	τ_{10}	$T_{\rm d}$[K]	$R_{\rm in}/R_\odot$	$M/M_\odot$
J052220.98	−0.50	5750	4500	0.015	220	2.63×10^5	0.9
J053250.69	−1.10	6000	5200	0.006	250	2.06×10^5	1.00
J004114.10	−1.04	5750	5800	0.007	280	1.65×10^5	1.00
J050632.10	−0.40	7600	6000	0.003	240	2.74×10^5	1.25
J003643.94	−0.63	7500	6500	0.002	250	2.56×10^5	1.50
J051848.84	−1.00	6000	6700	0.008	240	2.62×10^5	1.25
J004441.03	−1.07	6000	8500	0.002	320	6.64×10^4	2.00
J005803.08	−1.03	6500	12000	0.025	280	1.20×10^5	2.50
J045119.94	−0.40	8250	5000	0.006	270	2.97×10^4	0.80
J052241.52	−0.50	8250	5000	0.017	400	2.26×10^4	0.80
J052740.75	−0.50	8250	5200	0.024	470	1.22×10^4	0.90
J050221.17	−0.60	5250	4500	0.022	180	5.45×10^4	0.80
J051906.86	−1.30	5500	3800	0.015	180	5.13×10^4	0.65

Notes. The quantities listed in the various columns are the following: 1: Source ID; 2, 3: Metallicity and effective temperature derived spectroscopically by K14 and K15; 4–7: Luminosity, optical depth at 10 μm, dust temperature, and distance separating the central star from the inner border of the dusty region, found via SED fitting; 8: Mass of the progenitor at the beginning of the AGB phase, deduced via comparison of the derived luminosity with results from post-AGB evolution modelling.

is spherically distributed, and is characterized by a single dust component and temperature. Taking into account all these factors would not change the general conclusions drawn regarding the progenitors of the individual sources and the amount of dust in their surroundings, but would likely be reflected in the relative fractions of amorphous and crystalline silicates in the case of M-type sources.

The presence of crystalline silicate dust has so far been detected in AGB sources with optically thick dust envelopes in the Galaxy (Sylvester et al. 1999). Furthermore, emission bands associated with crystalline silicates in evolved stars in the LMC were studied by Jones et al. (2014), down to (gas) mass-loss rates of $\sim10^{-6}\,M_\odot\,{\rm yr}^{-1}$, fairly consistent with the mass-loss rates that low-luminosity, oxygen-rich stars attain at the tip of the

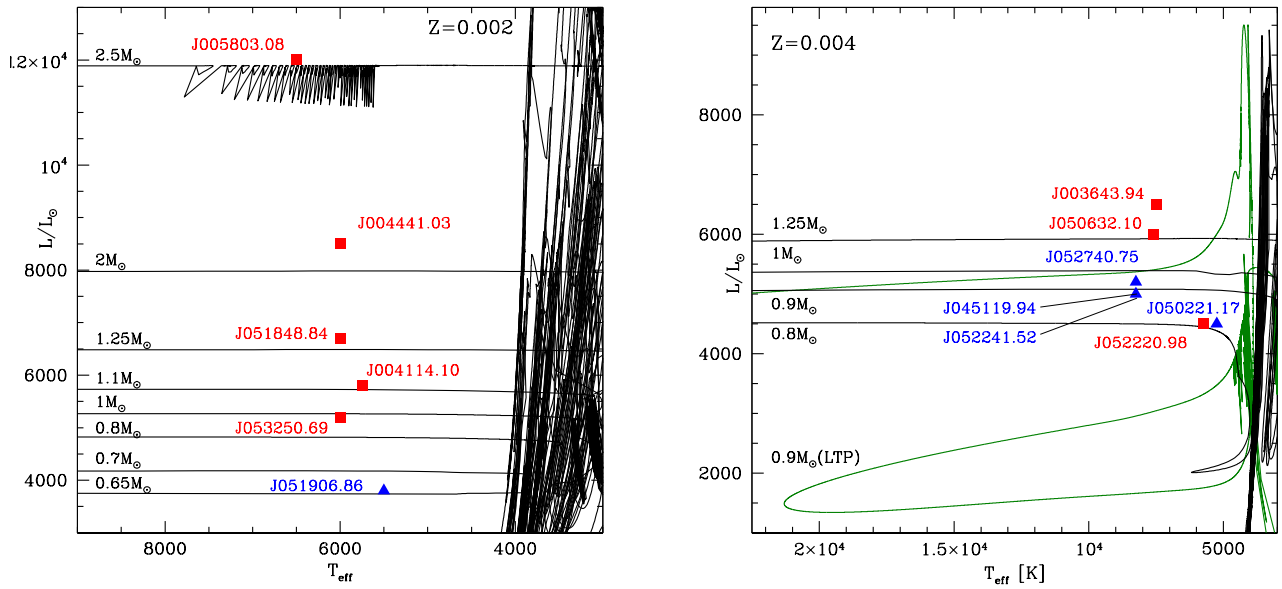

Fig. 3. Post-AGB evolutionary tracks of model stars of metallicity $Z = 2 \times 10^{-3}$ (*left panel*) and $Z = 4 \times 10^{-3}$ (*right*). The green track in the *right panel* refers to a 0.9 $M_{\odot}$ model star, which experienced a late TP, shortly after the beginning of the contraction towards the post-AGB phase. Coloured points indicate the observationally derived position of the sources considered in the present investigation, according to the effective temperatures given in K14 and K15, and the luminosities derived in Sect. 3. Red squares and blue triangles refer to the sources surrounded by carbonaceous dust and silicates, respectively.

AGB (see Sect. 6.5 below). The explanation proposed here holds as far as no change in the structure of silicate dust occurs as the dust moves away while the star contracts to the post-AGB phase.

4. The progenitors of the post-AGB-stars sample

We characterize the sources discussed in the previous section to infer the mass and formation epoch of the progenitors. To this end we consider the position of the stars on the Hertzsprung-Russell (HR) diagram, based on the values of effective temperature and luminosity listed in Table 1, and the evolutionary tracks of model stars of different mass, with the metallicity similar to those reported in Col. 2 of Table 1. This approach can be safely used in the case of post-AGB stars, given the peculiar morphology of the tracks, which run practically horizontally on the HR plane.

We show in Fig. 3 the position of the different sources on the HR diagram, overimposed on the evolutionary tracks of 0.65−2.5 $M_{\odot}$ stars[1]. We separate metal-poor sources, with [Fe/H] ~ -1, from the higher-metallicity counterparts. The former, reported in the left panel of Fig. 3, are compared with tracks of metallicity $Z = 2 \times 10^{-3}$, whereas to interpret the latter group, we use evolutionary sequences with metallicity $Z = 4 \times 10^{-3}$.

In the following paragraphs we present the interpretation of the stars, discussing separately the carbon stars and the oxygen-rich objects, grouped according to their estimated age and metallicity. When available, results from high-resolution spectroscopy, which allowed the determination of the surface chemical composition, will be compared with the expectations from stellar evolution modelling, thus providing a further test of the interpretation proposed here.

[1] The masses considered here refer to the beginning of the AGB phase, and thus they do not take into account possible mass loss during the RGB ascending.

4.1. Carbon stars

4.1.1. J053250.69 and J004114.10: low-mass, metal-poor carbon stars

The lowest-luminosity stars among the metal-poor objects surrounded by carbon dust are J053250.69 and J004114.10. From their position on the HR diagram, shown in the left panel of Fig. 3, we deduce that they descend from stars with mass equal to, or slightly greater than, 1 $M_{\odot}$. As far as J053250.69 is concerned, the presence of carbon dust is consistent with the results from van Aarle et al. (2013), which indicate that the surface chemistry is enriched in carbon. The surface C/O and [C/Fe] are in agreement with results from stellar evolution modelling: this is shown in Fig. 4, where the values given in van Aarle et al. (2013) are compared with the AGB time variation in the C/O ratio and in the surface carbon content of a 1 $M_{\odot}$ model star. The expected increase in the surface [O/Fe] (not shown in Fig. 4), of the order of 0.1 dex, is 0.1−0.2 dex below the lower limit given in van Aarle et al. (2013).

Regarding J004114.10, there are no results from spectroscopy. According to the estimated luminosity, we expect that the progenitor is ∼0.1 $M_{\odot}$ more massive than for J053250.69. In this case we expect a higher carbon enrichment, with a final [C/Fe] $\sim$ 1.5 (see right panel of Fig. 4).

Based on these results, and considering a 0.1−0.2 $M_{\odot}$ mass loss during the red-giant branch (RGB) ascending, we expect that these two sources descend from metal-poor progenitors of mass in the 1.2−1.3 $M_{\odot}$ range, born ∼3 Gyr ago.

4.1.2. J051848.84

For this source we derive a luminosity $L \sim 6700\,L_{\odot}$, consistent with the conclusions from De Smedt et al. (2015). This luminosity, as shown in the left panel of Fig. 3, corresponds to a ∼1.25 $M_{\odot}$ star. The conclusion drawn in Sect. 3, that the star is surrounded by carbon dust, is consistent with the discussion in De Smedt et al. (2015), that this source is enriched in

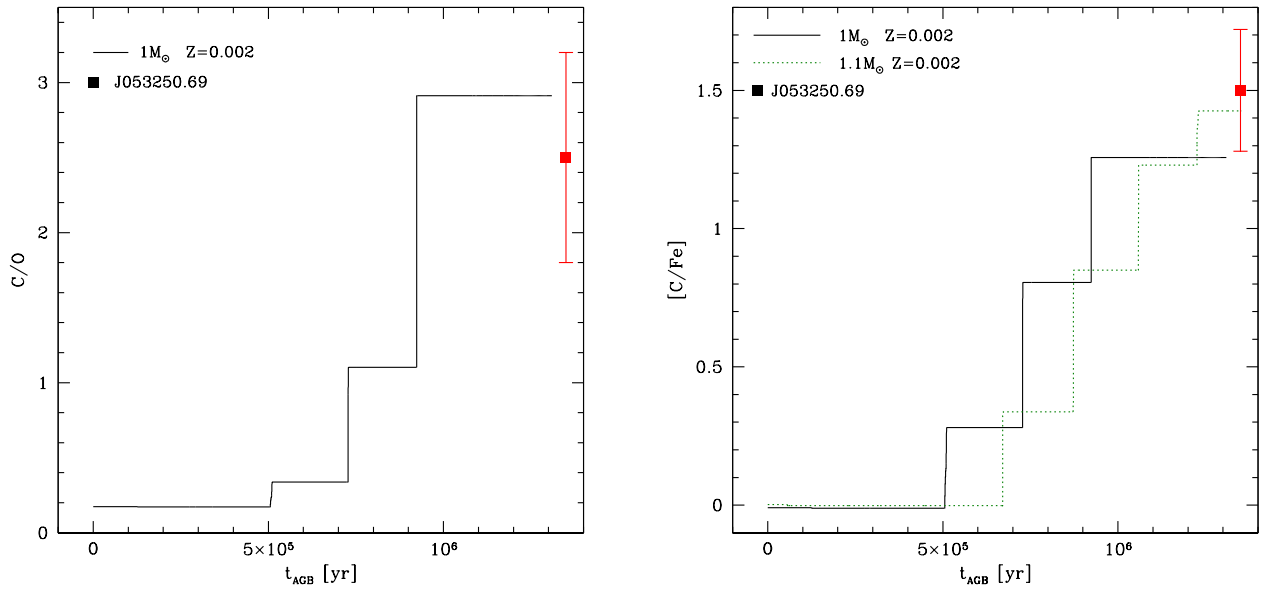

Fig. 4. The comparison between the surface chemistry of J053520.69 and the time variation of chemical composition of low-mass model stars. *Left*: time variation in the surface C/O ratio of a 1 $M_{\odot}$, metal-poor model star during the AGB phase, until post-AGB evolution. The red square and the red line indicate the measured value and the error bar from van Aarle et al. (2013). *Right*: time evolution of the surface carbon of two model stars of mass 1 $M_{\odot}$ (solid black line) and 1.1 $M_{\odot}$ (dotted green line), compared with results from van Aarle et al. (2013).

carbon, with [C/Fe] = 1.2. The *s*-process enrichment claimed by De Smedt et al. (2015) is a further hint of the action of repeated TDU events. The observed surface ^{12}C and ^{16}O are in agreement with results from stellar evolution modelling, as shown in Fig. 5, where the results from De Smedt et al. (2015) are compared with the time evolution of the surface carbon and oxygen of a 1.25 $M_{\odot}$ model star. Assuming a 0.1 $M_{\odot}$ mass loss during the RGB, we deduce that the progenitor of J051848.84 was a 1.3−1.4 $M_{\odot}$ star, which formed ∼2.5 Gyr ago.

4.1.3. J004441.03

This source, with an estimated luminosity of 8500 $L_{\odot}$, is among the brightest objects in the sample considered in the present investigation. We concluded in the previous section that it is surrounded by carbon dust: this is consistent both with the results from De Smedt et al. (2015), which indicate significant carbon and *s*-process enrichment, and with the interpretation based on the position on the HR diagram (see Fig. 3), which suggests a ∼2 $M_{\odot}$ progenitor. According to this understanding, this is the first source, among those discussed so far, that did not experience the helium flash, but rather core helium burning occurred in quiescent conditions of thermal stability. Stars of mass in the 2−3 $M_{\odot}$ range are expected to experience a series of TDU events that trigger a significant surface carbon enrichment: Dell'Agli et al. (2015a,b) concluded that the sources in the LMC exhibiting the largest IR excesses are the progeny of 2−3 $M_{\odot}$ stars.

This interpretation finds a confirmation in the results given in De Smedt et al. (2015), who find an extremely large surface carbon mass fraction [C/Fe] ∼ 1.7. The results shown in Fig. 6 confirm the robustness of the present analysis, as the final surface content of both carbon and oxygen are fully consistent with the values given by De Smedt et al. (2015). The estimated age of J004441.03 is ∼1 Gyr.

4.1.4. J005803.08

This is the brightest star in the sample, with an estimated luminosity of ∼12000 $L_{\odot}$. The comparison with results from post-AGB evolution modelling, shown in the left panel of Fig. 3, suggests that the progenitor of this source is a 2.5 $M_{\odot}$ star. The expected variation in the surface chemistry of such a star, in terms of the surface ^{12}C and ^{16}O mass fractions, is shown in Fig. 6, with dotted lines.

Similarly to the star examined previously, we expect that this source experienced several TDU events that caused a significant increase in the surface carbon, with a final [C/Fe] > 2. Some oxygen enrichment is also expected (see Fig. 6), as well as the increase in the *s*-process abundance. J005803.08 has the highest mass among the sources analysed here, and formed most recently, with an estimated age of slightly older than half a Gyr.

4.1.5. J050632.10 and J003643.94

From SED fitting (see Fig. 1) we find that both these sources with sub-solar chemical composition are surrounded by carbon dust. This is consistent with the estimated luminosities, in the 6000−6500 $L_{\odot}$ range, which, based on post-AGB modelling, correspond to progenitors of mass slightly above the solar mass (see right panel of Fig. 3), which are expected to experience a sufficiently large number of TDU episodes to reach the carbon star stage.

In their study, van Aarle et al. (2013) presented results from spectroscopy for J050632.10, which confirmed carbon enrichment, with [C/Fe] slightly above unity. As shown in Fig. 7, this is consistent with the expected carbon enrichment of 1.25 $M_{\odot}$ stars of metallicity Z = 0.004, which is the derived mass of the progenitor of this source, based on the luminosity. On the other hand, the expected oxygen enrichment is smaller than that indicated by van Aarle et al. (2013), even in the hypothesis that the gas from which the star formed was significantly α-enhanced, with [α/Fe] = +0.4.

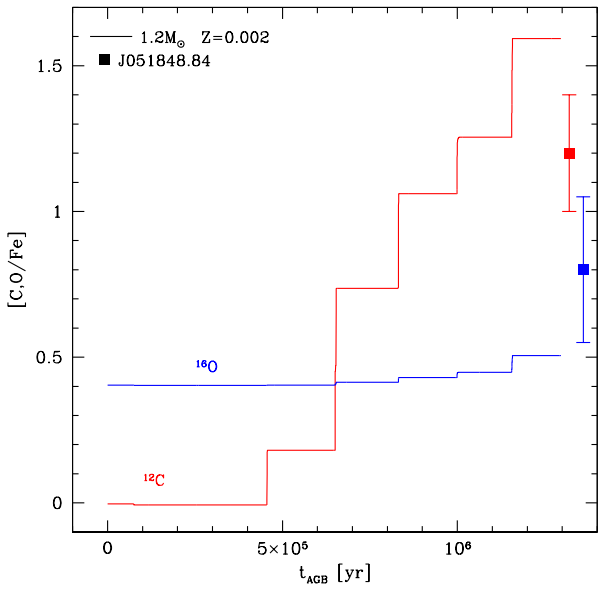

Fig. 5. Time variation in the surface carbon (red line) and oxygen (blue) content during the AGB evolution of a 1.25 $M_{\odot}$ model star of metallicity $Z = 0.002$. The red and blue points on the *right side* of the plane (with the corresponding error bars) indicate results for J051848.84 from De Smedt et al. (2015).

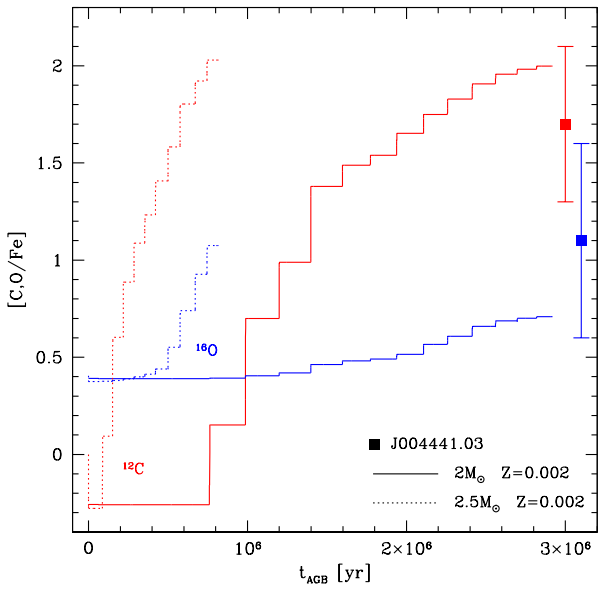

Fig. 6. Time variation in the surface carbon (red lines) and oxygen (blue) content during the AGB evolution of two $Z = 0.002$ model stars of mass 2 $M_{\odot}$ (solid lines) and 2.5 $M_{\odot}$ (dotted). The red and blue points on the right side of the plane (with the corresponding error bars) indicate results for J004441.03 from De Smedt et al. (2015).

J003643.94 is slightly brighter than J050632.10 (see right panel of Fig. 3), and thus we deduce a higher mass progenitor, with $M \sim 1.5\,M_{\odot}$. The results shown in Fig. 7, where the variation in the surface ^{12}C and ^{16}O for the 1.25 $M_{\odot}$ and 1.5 $M_{\odot}$ cases are reported, indicate that the final surface abundances of carbon and oxygen should be pretty similar to those found for J050632.10.

According to the present interpretation, the formation of J003643.94 occurred around 2 Gyr ago, whereas J050632.10 is older, with an estimated age slightly above 3 Gyr.

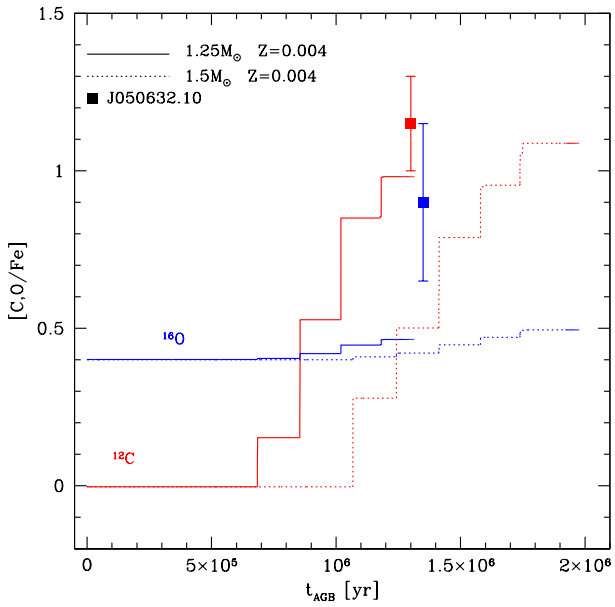

Fig. 7. Time variation in the surface carbon (red lines) and oxygen (blue) content during the AGB evolution of two $Z = 0.004$ model stars of mass 1.25 $M_{\odot}$ (solid lines) and 1.5 $M_{\odot}$ (dotted). The red and blue points in the *middle* of the plane (with the corresponding error bars) indicate results for J050632.10 from van Aarle et al. (2013).

4.1.6. J052220.98: a (too) faint carbon star

The position of J052220.98 on the HR diagram reported in the right panel of Fig. 3 suggests a ~0.8 $M_{\odot}$ progenitor, an interpretation that, however, is at odds with the analysis in Sect. 3, where we found that this source is surrounded by carbon dust. Indeed, as discussed earlier in this section, we expect that carbon stars of metallicity similar to J052220.98 evolve to the post-AGB phase with luminosities above ~5000 $L_{\odot}$, which translates into $M > 0.9\,M_{\odot}$ progenitors.

A possible explanation for this apparently anomalous behaviour is that J052220.98 descends from a low-mass progenitor, which experienced an extraordinary deep TDU event during the late evolutionary phases: the consequent large carbon enrichment would have turned the star into a carbon star. While this possibility cannot be ruled out, we are more predisposed to considering the hypothesis that this source experienced a late thermal pulse (TP) shortly after the beginning of the contraction towards the post-AGB post-AGB phase. The idea that helium ignition might occur after the stars leave the AGB was proposed by Iben et al. (1983) and then further investigated by Blöcker (2001), who studied different cases, distinguished by the time after the beginning of the overall contraction when the late TP is ignited. In particular, in the late TP case discussed by Blöcker (2001), the evolutionary tracks are characterized by a first excursion to the blue, followed by the expansion to the red, before the standard post-AGB contraction begins. An example of such behaviour is reported in the right panel of Fig. 3, in which the green line refers to the evolution of a 0.9 $M_{\odot}$ model star that underwent helium ignition immediately after the start of the overall contraction.

During the occurrence of the loop, the luminosity of the star is fainter than expected on the basis of the classic core mass - luminosity relationship. We therefore suggest that J052220.98 descends from a ~0.9−1 $M_{\odot}$ progenitor that reached the C-star stage during the AGB, and is now evolving through a loop

similar to the one shown in the figure, after having experienced a late TP.

4.2. Oxygen-rich stars

Five of the sources investigated here show evidence of silicate dust in their surroundings, based on the analysis presented in Sect. 3. These stars are indicated with blue triangles in Fig. 3.

A first possible explanation for these objects is that they descend from $M > 3\,M_{\odot}$ stars, which experienced HBB during the AGB phase; the latter mechanism prevents surface carbon enrichment, owing to the proton-capture activity experienced at the base of the convective envelope, which depletes the surface ^{12}C. This option can be safely ruled out in the present case, as such massive AGB stars are expected to enter the post-AGB phase with luminosities not below $20\,000\,L_{\odot}$, and thus significantly higher than those of the stars considered here, as is clear in Fig. 3.

An alternative explanation is that these sources are the progeny of low-mass stars that failed to reach the C-star stage. For a given metallicity, a luminosity threshold exists, separating carbon stars from their lower-mass (and fainter) counterparts that evolve as oxygen-rich objects: indeed the latter stars at the beginning of the AGB phase are composed of a $\sim$0.5 $M_{\odot}$ degenerate core and of a convective envelope of a few tenths of solar mass that is lost via stellar winds before the number of TDUs required to reach the carbon star stage is experienced. The luminosity threshold is sensitive to the metallicity, as the achievement of the C-star stage is easier the lower the metallicity, owing to the smaller amount of oxygen in the envelope of the star. In the $Z = 0.002$ case, we find that carbon stars should have $L > 4700\,L_{\odot}$, whereas for $Z = 0.004$, the threshold luminosity is $\sim$5200 $L_{\odot}$.

The luminosities of the five sources characterized by the presence of silicate dust in their surroundings are within the limits given above, as shown in Fig. 3. In particular J051906.86 and J050221.17 are significantly fainter than the threshold luminosities discussed above. Thus, they are interpreted as the progeny of low-mass stars, with mass at the beginning of the AGB phase of $\sim$0.7 $M_{\odot}$ (J051906.86) and $\sim$0.8 $M_{\odot}$ (J050221.17), respectively, which, by assuming a typical RGB mass loss of 0.1$-$0.2 $M_{\odot}$, correspond to ages in the 8 $-$ 10 Gyr range. These are the oldest objects in the sample investigated here.

On the other hand, J052740.75, J045119.94, and J052241.52 are slightly brighter, with luminosities close to the previously discussed threshold, holding for the $Z = 0.004$ population. These luminosities correspond to $\sim$0.85 $M_{\odot}$ progenitors that formed between 6 and 8 Gyr ago. We might expect to observe some carbon and *s*-process enrichment at their surface, as it is likely that they experienced some TDU events before their entire envelope was lost.

5. Dust production during the late-AGB phases

During AGB evolution the stars gradually lose their external convective mantle. While the central regions contract, the external layers become increasingly less bound on the gravitational side to the compact core and expand, and the mass-loss rate is consequently enhanced. This general rule holds for low-mass objects that evolve as M-type stars, such as those discussed in Sect. 4.2, and even more for carbon stars: indeed in the latter case, the expansion of the structure is further favoured by the rise in the surface carbon, which is accompanied by a significant increase in the molecular opacities (Marigo 2002). Massive AGB stars that experience HBB follow a different behaviour, as in this case the largest mass-loss rates are experienced during the phases when HBB is strongest (Ventura et al. 2015), which happens before a significant fraction of the envelope is lost. However, this is not relevant in the present context, as we showed in Sect. 4 that the post-AGB stars discussed here descend from $M < 3\,M_{\odot}$ progenitors.

The above arguments indicate that the final AGB phases are the most relevant in order to understand dust production from stars. This is because most of the mass is lost during the last interpulse phases and the dust-production rate, tightly correlated with $\dot{M}$, increases rapidly towards the end of AGB evolution. Understanding dust production during the tip of the AGB (TAGB, i.e. the phase preceding the beginning of the contraction of the star towards the post-AGB), is therefore crucial in order to evaluate the dust yields from single stars and the overall contribution from these objects to dust production in the host system. Indeed the total dust-production rate of some galaxies is mostly determined from a low fraction of AGB stars, which are currently evolving through the very final AGB phases (Dell'Agli et al. 2016, 2018, 2019). In addition, the comprehension of the TAGB later is crucial to interpret the distribution of stars of galaxies in the observational colour-colour and colour-magnitude planes, because it is when they are evolving thorugh the TAGB that the stars are expected to exhibit the largest IR excesses, and thus the reddest IR colours (Marini et al. 2021; Dell'Agli et al. 2021).

Figure 8 shows the mass-loss rate at the TAGB, $\dot{M}^{\rm TAGB}$, calculated via stellar evolution modelling, as a function of the mass of the star at the beginning of the AGB phase. $\dot{M}^{\rm TAGB}$ increases with stellar mass, as higher-mass stars reach higher luminosities and radii. The steep rise in $\dot{M}^{\rm TAGB}$, corresponding to the threshold mass at which the transition from M-type to C-stars takes place, which is connected to the previously discussed increase in the surface molecular opacities that takes place when C-rich molecules form, is evident in the figure.

In the following section, we critically evaluate the mass-loss rates reported in Fig. 8 by comparing the theoretical expectations regarding the dust in the surroundings of post-AGB stars with the results discussed in Sects. 3 and 4. In this regard, we consider the characterization of the individual sources presented in Sect. 4, which allows the derivation of the mass of the progenitors and, based on the results shown in Fig. 8, of $\dot{M}^{\rm TAGB}$. These rates, properly scaled with the effective temperature, lead to the determination of the variation in the mass-loss rates experienced by the stars during the contraction to the post-AGB phase.

The comparison with the results deduced in Sect. 3, particularly with the derived values of τ_{10}, allows us to test the $\dot{M}^{\rm TAGB}$ values reported in Fig. 8 and, at the same time, to identify the evolutionary phase when the dust responsible for the currently observed IR excess was released. For this, we concentrate on some specific points distributed along the post-AGB evolutionary tracks, each identified by the value of the effective temperature. For each of these points, we derive $\tau_{10}^{\rm onset}$, the optical depth that characterizes the SED of the star if it was observed during the evolutionary stage considered. The values of $\tau_{10}^{\rm onset}$ are calculated on the basis of stellar evolution + dust-formation modelling, and the application of Eq. (3).

We note that the possibility that dust production continues after the beginning of the contraction to the post-AGB was already considered, for example by van Hoof et al. (1997), who explored both the possibilities that dust formation ceases after the AGB, or that it carries on during the post-AGB phase. In the following section we show that for all the sources considered, the

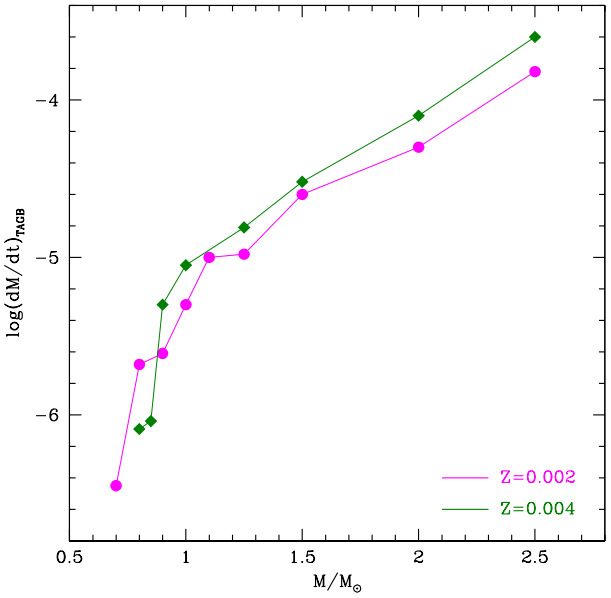

Fig. 8. Mass-loss rate at the tip of the AGB for stars of different mass, reported on the abscissa, and metallicity $Z = 0.002$ (magenta points), and $Z = 0.004$ (green diamonds). The values reported in the plane were calculated by stellar evolution modelling.

observations are not consistent with the possibility that the dust was released after the effective temperatures rose above 4000 K. Therefore, here we do not explore dust formation during the post-AGB phase through which the sources are evolving nowadays, but rather we consider the possibilities that formation of dust was halted either at the tip of the AGB or during the early phases after the beginning of the contraction to the post-AGB phase.

The second step will consist in the determination of $\tau_{10}^{\rm now}$, the optical depth that characterizes the current SED of the star, if the dust was released during the stages for which $\tau_{10}^{\rm onset}$ was calculated. To this end, we consider the general expression given by Eq. (3). In the computation of the integral on the right-hand side, most of the contribution comes from the regions close to the inner border of the dusty layer, as $n_{\rm d}$ decreases with distance: therefore, τ_{10} is mainly determined by the thermodynamic conditions, particularly the density, at the distance $R_{\rm in}$ from the centre of the star. Assuming that $n_{\rm d}$ scales as r^{-2}, and that Q_{10} and a do not change as the dust moves outwards, we find that the optical depth found via Eq. (3) scales as $R_{\rm in}^{-1}$.

Regarding the tip of the AGB or the different post-AGB phases taken into account, we consider that both solid carbon dust and silicates form at a distance of $\sim 10 R_*$ (Dell'Agli 2012), and thus $\tau_{10}^{\rm onset} \sim (10R_*)^{-1}$. Regarding the dust presently surrounding the star, located at a distance $R_{\rm in}$, we have $\tau_{10}^{\rm now} \sim R_{\rm in}^{-1}$. Therefore, the relation we are looking for is

$$\tau_{10}^{\rm now} \sim \tau_{10}^{\rm onset} \times (10R_*/R_{\rm in}). \quad (4)$$

The comparison between the values of the optical depth derived via Eq. (4) and those found in Sect. 3 enables testing of the different hypothesis considered. The methodology followed in order to understand how dust formation and mass loss work during the final AGB phases, and during the beginning of the post-AGB contraction, are also based on the analysis of the derived expansion velocities with which the dust layer would travel from the evolutionary stage when it was released until now, in turn calculated based on the derived distance of the dusty region and the time elapsed, found via the modelling of the AGB and post-AGB phases. Our reference point is that the wind velocity during the post-AGB phase is generally assumed to be comparable with the velocity in the AGB phase, with values that typically span the $10-30\,{\rm km\,s^{-1}}$ range (He et al. 2014; Klochkova et al. 2015).

Whenever the results from this analysis prove unsatisfactory, we model post-AGB evolution by adopting different mass-loss rates, in an attempt to understand when the dust responsible for the observed IR excess of the various sources was released, and to derive the post-AGB mass loss that would determine evolutionary timescales consistent with the dynamical conditions expected.

6. Dust formation and wind propagation across the AGB-post-AGB frontier

A summary of the results derived in Sect. 3 from the interpretation of the optical and IR data of the stars considered are presented in Fig. 9, which shows τ_{10} of the individual sources as a function of the luminosity (left panel) and of the distance of the inner border of the dust layer from the centre of the star (right). Different trends can be detected in the figure, which correlate τ_{10} with the stellar luminosity and dust mineralogy for stars of different metallicity.

Concerning metal-poor carbon stars (full, red squares in the figure), we note: a) the correlation between luminosity and optical depth (left panel), with the brighter stars exhibiting larger IR excesses; and b) luminosity and $R_{\rm in}$ are anti-correlated, the brighter the star, the closer the inner border of the dusty layer is to the surface.

The metallicity of the stars also plays a role in the present context: the two higher-metallicity carbon stars, indicated with open squares in Fig. 9, are characterized by optical depths significantly smaller than their lower-metallicity counterparts with similar luminosities.

The oxygen rich stars behave differently from carbon stars. The former are characterized by similar luminosities (see Fig. 3), and optical depths extending over a factor of roughly two with respect to the average value $\tau_{10} = 0.02$. Inspection of the right panel of Fig. 9 shows that the dusty zones for oxygen rich stars are closer than those for carbon stars.

To explain these trends, and to have a more exhaustive view of dust production and propagation during the phases from the tip of the AGB until the present time, we apply the methodology described in the previous section, to study in detail a few objects, selected among those discussed in Sect. 3, which are diverse in luminosity and dust composition. The sources selected are J005803.08, J053250.69, and J050221.17. The first object, discussed in Sect. 4.1.4, is a bright carbon star, which experienced several TDU episodes that were responsible for the significant carbon enrichment in its surface regions. J053250.69, discussed in Sect. 4.1.1, is representative of faint, low-mass carbon stars that reached the C-star stage during the last thermal pulses. J050221.17 is a low-mass, oxygen-rich star that failed to become a carbon star because the number of TDU events experienced (if any) was not sufficient to reach the C/O > 1 condition. We also discuss two carbon stars with sub-solar chemical composition, and J052220.98, the low-luminosity carbon star, for which a possible characterization was presented in Sect. 4.1.6.

6.1. Bright post-AGB stars with carbon dust

According to the discussion in Sect. 4.1.4, J005803.08 is the brightest source investigated, with a luminosity of $\sim 12\,000\,L_\odot$,

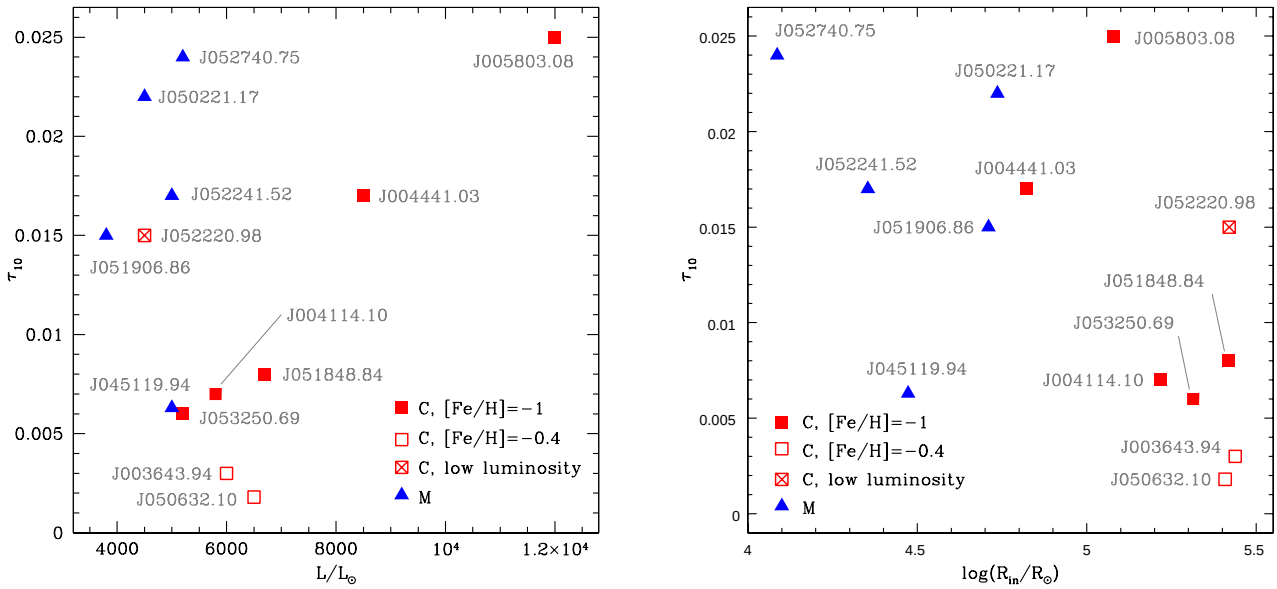

Fig. 9. Optical depth of the different sources obtained from the SED fitting in Sect. 3 as a function of the luminosity of the stars (*left panel*) and of the distance of the internal border of the dusty region from the centre of the star (*right*). Red squares and blue triangles indicate stars surrounded by carbonaceous dust and silicates, respectively. Crossed red squares refer to stars exhibiting evidence of carbon dust, despite their luminosities being consistent with an M-type nature.

which indicates a ~2.5 $M_\odot$ progenitor. This is close to the threshold limit required to start HBB (Ventura et al. 2013), which destroys the surface carbon and prevents the C-star stage. As the luminosity of the star increases with the initial mass (see e.g. Fig. 3), we argue that J005803.08 is among the brightest post-AGB stars with a carbon-star chemistry.

The AGB evolution of these stars was studied in detail by Dell'Agli et al. (2015a) and more recently by Marini et al. (2021), who outlined the large quantities of carbon accumulated in the surface regions and the intense dust production taking place, particularly during the very final AGB phases. Results from stellar evolution and dust-formation modelling suggest that at the tip of AGB, this class of stars experiences mass-loss rates slightly in excess of $10^{-4}\,M_\odot\,\mathrm{yr}^{-1}$ and efficient dust production, with rates of the order of a few $10^{-6}\,M_\odot\,\mathrm{yr}^{-1}$; a thick dust shell composed mainly of solid carbon is expected to surround the star while evolving at the TAGB, with optical depths of $\tau_{10} \sim 5$ (Dell'Agli et al. 2021). At solar or sub-solar chemistries, SiC grains might offer a significant contribution to the overall extinction of the radiation, but this is not the case for J005803.08, owing to its low metallicity.

Figure 10 shows the time evolution of the effective temperature of a 2.5 $M_\odot$ model star of metallicity similar to that of J005803.08, starting from the latest AGB phases through the contraction to the post-AGB phase. The standard evolution, represented by the black line in the figure, was obtained with the input physics specified in Sect. 2 for the AGB and the post-AGB phases. In this case the time elapsed from the tip of the AGB until the current evolutionary stage, at $T_{\rm eff} = 6500$ K (see Table 1), is ~5600 yr.

For the tip of the AGB and for five further evolutionary phases selected during the post-AGB, corresponding to effective temperatures in the 3000 K $< T_{\rm eff} <$ 5000 K range, equally spaced by 500 K, we calculated the optical depth $\tau_{10}^{\rm onset}$. The results are shown in Fig. 11. $\tau_{10}^{\rm onset}$ decreases as the star contracts (and the effective temperature increases), since the mass-loss rate diminishes, and thus the wind is less dense (see Eq. (2)), so lower amounts of gas molecules are available to condense into dust.

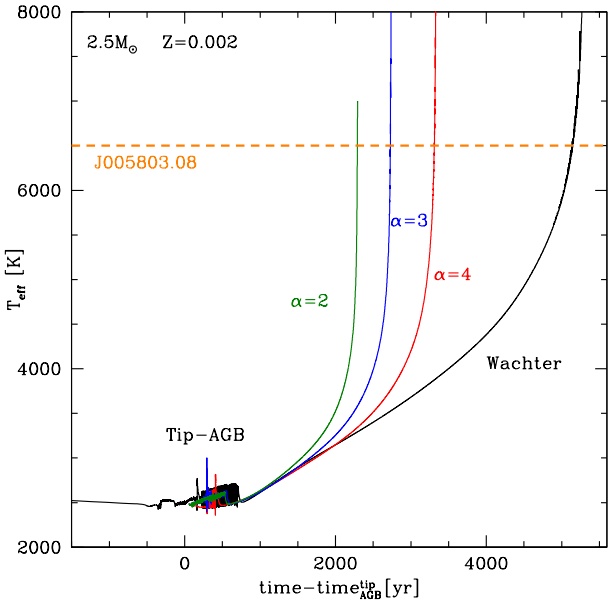

Fig. 10. Time variation in the effective temperature of a 2.5 $M_\odot$ model star during the transition from the AGB to the post-AGB phase. Times are counted since the beginning of contraction. The black line indicates the standard result, obtained by adopting the prescription from Wachter et al. (2002, 2008) for mass loss. Coloured tracks refer to results obtained by assuming that $\dot{M}$ decreases as $T_{\rm eff}^{-\alpha}$, with $\alpha = 2$ (green), 3 (blue) and 4 (red). The dashed orange line indicates the effective temperature of J005803.08 given in K14 and K15.

We followed the approach described in the previous section to calculate the corresponding $\tau_{10}^{\rm now}$ for each of the phases considered. We limited this analysis to the phases with $T_{\rm eff} \leq 4000$ K, because dust production during later phases is too small to account for the IR excess observed (see Fig. 11). To calculate $\tau_{10}^{\rm now}$ via Eq. (4), we used the distance of the inner border of the dusty zone derived in Sect. 4.1.4 for J005803.08, namely $R_{\rm in} = 1.2 \times 10^5\,R_\odot$, and the radius and optical depth corresponding to each

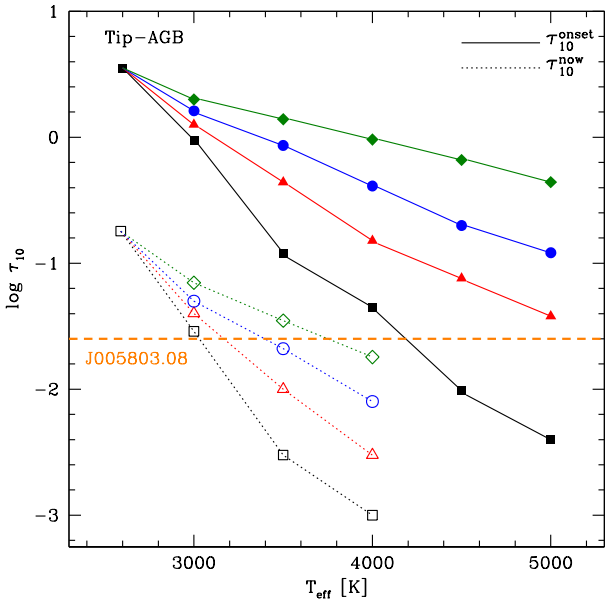

Fig. 11. Solid lines and full points indicate the values of the optical depth τ_{10}^{onset} that characterize dust production at the tip of the AGB and during different phases along the contraction sequence of a 2.5 $M_{\odot}$ model star (see text for details). The colours used correspond to different treatments of mass loss, following the same colour coding as in Fig. 10. Dotted lines and open symbols indicate the values of the optical depth τ_{10}^{now} that would characterize the dust responsible for the IR excess observed nowadays, at the effective temperature of J005803.08 (6500 K), under the assumption that it was released while the star was evolving through the evolutionary stages with the effective temperatures reported on the abscissa. The dashed orange line represents the optical depth obtained for J005803.08 from SED fitting.

evolutionary phase. The results, indicated by black, open squares in Fig. 11, are connected with a dotted line.

We are predisposed to ruling out the possibility that the dust observed in the surroundings of J005803.08 was released while the star was evolving at the tip of the AGB, for the following reasons: a) the expected τ_{10} is a factor of roughly seven higher than that derived from SED fitting; and b) if we estimate the average expansion velocity with which the dust would have travelled away from the star, on the basis of R_{in} and of the time elapsed since the tip of the AGB to the current evolutionary status, we obtain $v \sim 0.5\,km\,s^{-1}$, which is much lower than observed (He et al. 2014; Klochkova et al. 2015).

In the context of the results obtained with the input given in Sect. 2 (black squares in Fig. 11), the only possibility consistent with the analysis in Sect. 3 is that the dust observed now was released after the beginning of the contraction to the post-AGB phase, when the effective temperature of the star was ∼3000 K. On the other hand we can rule out this possibility too, because the time elapsed since the evolutionary phase considered is ∼3600 yr, which, combined with the distance of the dusty layer, leads to an average expansion velocity below $1\,km\,s^{-1}$, which is still too small. As a further motivation to disregard this possibility, we consider that if the winds and the dust move with a $\sim 0.8\,km\,s^{-1}$ velocity, the dust produced at the tip of the AGB would now be at a distance $\sim 2R_{in}$, and would determine the formation of a bump in the SED of the star in the 25−30 μm region, which is not observed.

As we could not obtain any satisfactory overall explanation for the observations of J005803.08, we explored different mass-loss-rate laws by changing the slope of $\dot{M}$ with the effective temperature with respect to the treatment by Wachter et al. (2002, 2008), according to which $\dot{M} \sim T_{eff}^{-7}$. We calculated new evolutionary sequences for the 2.5 $M_{\odot}$ model star, starting from the tip of the AGB, where we left the mass-loss rate $\dot{M}^{TAGB}$ unchanged, then extended to the post-AGB, during which we assumed $\dot{M} = \dot{M}^{TAGB} \times (T_{eff}/T_{eff}^{TAGB})^{-\alpha}$, with $\alpha = 2, 3, 4$. The results of these runs are reported in Fig. 10, which shows the time variation in the effective temperature, and in Fig. 11, reporting the corresponding optical depths, with a different colour coding. The evolutionary timescales get shorter the higher the mass-loss rate, as the rate of the contraction process during the AGB to post-AGB transition is determined by the rate with which the residual envelope is lost (Iben & Renzini 1983). The impact of the treatment of mass loss on the timescales of the AGB to post-AGB transition was studied by van Hoof et al. (1997), who showed that the rate at which the effective temperatures of post-AGB stars increase gets significantly shorter when it is assumed that the mass-loss rate remains high after the contraction phase begins.

Consistency between the expected and the observed IR excess (and thus optical depth) is found in the $\alpha = 2$ and $\alpha = 3$ cases, if we assume that the dust observed now was released when the star contracted until the evolutionary phase characterized by effective temperatures in the 3500−4000 K range. In these cases the derived average expansion velocity of the wind is in the $5-20\,km\,s^{-1}$ range, and thus consistent with the observational evidence (He et al. 2014; Klochkova et al. 2015). Furthermore, these velocities are sufficiently fast that the dust released at the tip of AGB would in the meantime reach regions $5-20R_{in}$ away from the central star, thus having no effect on the SED in the $\lambda < 50\,\mu m$ spectral region. In summary, the interpretation of the observations of J005803.08 indicate that mass-loss rates of bright carbon stars evolving at the tip of the AGB slightly in excess of $10^{-4}\,M_{\odot}\,yr^{-1}$ are consistent with the IR excess observed, provided that we assume that the dust was released when the effective temperatures reached ∼3500−4000 K, and that the rate of mass loss during the transition to the post-AGB scales as T_{eff}^{-2}.

6.2. Low-mass carbon stars

J053250.69 is the faintest among the stars that we interpret as surrounded by carbon dust, shown in Fig. 3, with the sole exception of J052220.98, which is discussed in a separate section. In Sect. 4.1.1 we interpreted this object as descending from a low-mass progenitor, with mass at the beginning of the AGB phase of the order of 1 $M_{\odot}$. This mass is close to the lower threshold required to reach the C-star stage. As shown in Fig. 4, which reports the time variation in the surface C/O and [C/Fe] of a 1 $M_{\odot}$ model star with the same metallicity of J053250.69, the C-star stage is reached during the last two TPs. The expected mass-loss rate at the tip of the AGB is $\dot{M}^{TAGB} \sim 10^{-5}\,M_{\odot}\,yr^{-1}$ (see Fig. 8). By studying this source, we are exploring the low-luminosity tail of the carbon star population in such a way that the study of this star, coupled with the analysis of J005803.08 done previously, allows a thorough view of the late-AGB and post-AGB evolution of carbon stars.

In analogy with the analysis of J005803.08, we considered the tip of the AGB and different phases during the transition to the post-AGB phase of a ∼1 $M_{\odot}$ model star, characterized by specific values of the effective temperature, selected in the 3500−5000 K range, spaced by 500 K. We used the same methods described earlier to calculate τ_{10}^{onset} for these stages. This

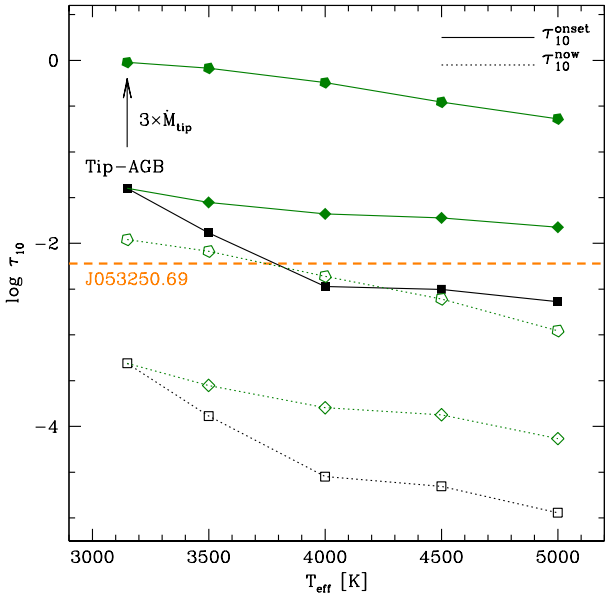

Fig. 12. Variation with the effective temperature of the optical depth, characterizing various evolutionary phases of a 1 $M_\odot$ model star, from the tip of the AGB (first point on the plane) to the post-AGB. Full squares connected with solid lines indicate the values of τ_{10}^{onset} obtained with the physical ingredients discussed in Sect. 2 to model the evolution of the star, whereas open squares refer to the expected optical depths that would be observed in the present epoch, τ_{10}^{now}. Full and open diamonds refer to the results obtained by assuming a different scaling of mass loss with the effective temperature during the contraction to the post-AGB phase (see text for details). Green pentagons indicate the optical depths obtained by artificially increasing the mass-loss rate at the tip of AGB by a factor of three. The dashed orange line indicates the optical depth of J053250.69, obtained by SED fitting.

analysis was applied both to the standard evolution of the 1 $M_\odot$ model star used to study J053250.69, with the mass-loss description by Wachter et al. (2002, 2008), and to the case where the post-AGB mass-loss rate is assumed to change as $\dot{M} = \dot{M}^{TAGB} \times (T_{eff}/T_{eff}^{TAGB})^{-2}$.

The results of this exploration are reported in Fig. 12, which shows with full symbols the values assumed by the optical depth characterizing the SED of the star as it evolves from the tip of the AGB (first point on the left side of the figure) to the post-AGB phase. The corresponding values assumed by the optical depth in the present epoch, under the hypothesis that the dust was released during the evolutionary phases considered, are indicated with open symbols. The results obtained by standard evolution modelling and those based on the $\dot{M} \sim T_{eff}^{-2}$ law are indicated in Fig. 12 with black squares and green diamonds, respectively.

We see in Fig. 12 that the optical depths obtained are significantly smaller than those derived for J053250.69, the differences exceeding a factor of ten in all cases. This conclusion holds independently of the treatment of the mass loss adopted to describe the contraction to the post-AGB phase.

A further issue is related to the estimated velocities with which the dusty layer has moved away from the star since it was released, until present times. According to the standard description of the transition from the tip of the AGB to the post-AGB phase, the expected time transcribed from the tip of the AGB to the current phase would be ∼15 000 yr; this result, combined with the distance of the dusty region derived in Sect. 3, namely $2 \times 10^5\,R_\odot$, corresponds to an average expansion velocity below 1 km s^{-1}. Even if we assume that the dust was released during a later evolutionary phase, for instance when the effective temperature was 4000 K (although that is highly inconsistent with the estimated optical depth), the average expansion velocity would not exceed 1 km s^{-1}.

The conclusion drawn from this preliminary analysis is that the mass-loss rate at the tip of the AGB of low-mass carbon stars is underestimated. A higher $\dot{M}^{TAGB}$ is required not only to obtain higher optical depths, compatible with the IR excess observed, but also to shorten the contraction timescales, so that the derived velocities are consistent with the observations (He et al. 2014; Klochkova et al. 2015).

Based on these arguments, we calculated additional evolutionary sequences starting from the tip of the AGB, through the contraction to the post-AGB phase, until reaching the effective temperature of J053250.69. In these computations $\dot{M}^{TAGB}$ was artificially enhanced with respect to the $\sim 10^{-5}\,M_\odot\,yr^{-1}$ value given above, and the mass-loss rate during the following contraction phases was changed accordingly, either by assuming the recipe by Wachter et al. (2002, 2008), or by adopting the $\dot{M} \sim T_{eff}^{-2}$ relationship.

The results obtained by adopting a factor of three increase in $\dot{M}^{TAGB}$ and $\dot{M} \sim T_{eff}^{-2}$ for the following phases are indicated with green pentagons in Fig. 12. Consistency between the derived and the expected optical depth is obtained when assuming that the dust responsible for the currently observed IR excess was released when the effective temperature of the star was 3500−4000 K. In this case the time interval is reduced to 500−1000 yr, and thus the average expansion velocity of the wind is between 10 and 15 km s^{-1}.

We restrict our attention to the $\alpha = -2$ case. Indeed, if we use the scaling of mass loss with effective temperature described in Sect. 2, the only possibility to obtain an IR excess comparable to the observed one is that the dust was released while the star was at the tip of the AGB. However, in that case the dust would have travelled for ∼5000 yr, and thus the average expansion velocity would be of the order of 1 km s^{-1}.

6.3. Carbon stars with sub-solar chemistry

The carbon-stars sample studied here encompasses J050632.10 and J003643.94, two sub-solar metallicity stars with similar luminosities, around 6000 $L_\odot$ (see Table 1 and right panel of Fig. 3). In Sect. 4.1.5 we suggest that these stars descend from ∼1−1.5 $M_\odot$ progenitors, which became carbon stars.

Both stars, indicated with open, red squares in Fig. 9, fall off the τ_{10} versus luminosity trend defined by low-metallicity carbon stars, as their optical depths are approximately two times smaller. Moreover, the current distances of the dusty region from the central star are the largest among the stars in the whole sample.

These differences can be at least partly explained by the fact that these two stars are the hottest among the carbon stars considered, as reported in Table 1. This indicates that they are evolving through a more advanced post-AGB phase than the carbon stars of lower metallicity. This allowed the dusty layer to travel further away and reach larger distances.

However, the previous arguments alone are not sufficient to account for the low IR excess observed in the SEDs of J050632.10 and J003643.94. Indeed, as shown in the right panel of Fig. 9, the distances of the dusty regions around these two sources are found to be ∼0.05−0.1 dex higher than in the other carbon stars: by applying Eq. (4), we find that the corresponding differences in τ_{10}^{now} are not expected to exceed 20−30%. To recover the difference of a factor of roughly two in the derived

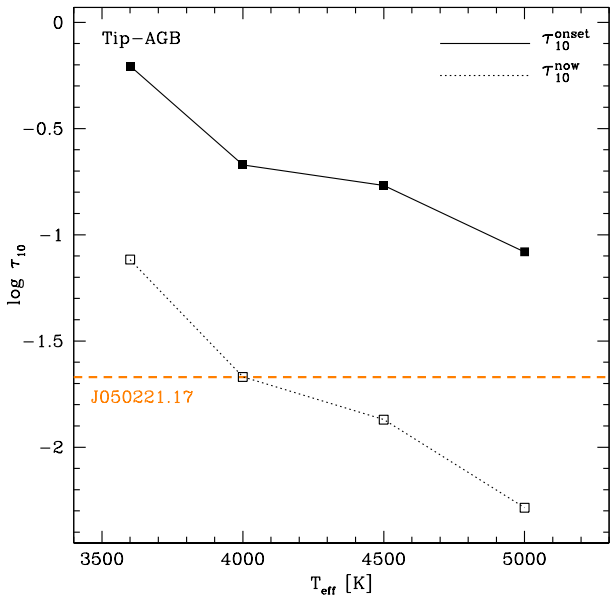

Fig. 13. Variation with the effective temperature of the optical depth characterizing various evolutionary phases of a 1 $M_{\odot}$ model star, from the tip of the AGB (first point on the plane) to the post-AGB phase. Full squares connected with solid lines indicate the values of τ_{10}^{onset} obtained with the physical ingredients discussed in Sect. 2 to model the evolution of the star, whereas open squares refer to the expected optical depths that would be observed in the present epoch, τ_{10}^{now}. The dashed orange line indicates the optical depth of J050221.17, obtained by SED fitting.

optical depth, we must assume that dust formation during the late evolutionary phases was significantly less efficient.

The most plausible explanation for the lower dust formation that J050632.10 and J003643.94 experienced during the late-AGB phases is the smaller number of gaseous carbon molecules available to condense into solid particles in the surface regions, in turn related to the small carbon excess with respect to oxygen. Indeed, the latter is the relevant quantity for the formation of solid carbon dust, given the high stability of CO molecules (Ferrarotti & Gail 2006). The carbon excess is intrinsically larger in metal-poor stars ($Z \sim 0.004$), given the lower initial oxygen content, while it is smaller in stars with sub-solar chemistry, as for the two sources investigated here. This quantity is also sensitive to any possible oxygen enrichment connected to the TDU events experienced.

The latter point deserves particular attention. The results shown in Fig. 7 indicate that negligible oxygen enrichment is expected to have taken place in the surface regions of these two stars. On the other hand, van Aarle et al. (2013) claim significant oxygen enrichment for J050632.10, which implies a low carbon excess, and consequently poor dust production. We conclude that the low IR excess characterizing the two stars considered is related to the metallicity and to the oxygen enrichment, witnessed by results from high-resolution spectroscopy.

There are some implications related to these results, which will deserve further investigations in the future. First, the observations of J050632.10, similarly to other post-AGB stars in the Milky Way (Kamath et al. 2021), outline a significant enrichment in the surface oxygen, which is not expected based on the current modelling of the AGB phases. Regarding the description of mass loss of carbon stars, the formalism must include some sensitivity to the surface chemical composition, as the efficiency with which the winds of carbon stars are radiatively driven by dust is highly sensitive to the carbon excess with respect to oxygen. Finally, in the description of carbon dust formation, it is recommended that the number density of seeds over which the dust grains grow, as suggested by Nanni et al. (2013, 2014), is taken as dependent on the carbon excess, instead of assuming a plain proportionality to the hydrogen density, as is done in most of the descriptions currently used.

6.4. A faint, dusty C-star

In the left panel of Fig. 9, we note the anomalous position of J052220.98, which falls off the general trend defined by C-stars: despite its low luminosity, which is the smallest among the carbon stars in the sample, its optical depth derived in Sect. 3 is similar to the brightest carbon stars considered.

In Sect. 4.1.6 we discussed the possible origin of this object and proposed that it experienced a late TP, which is the reason for the relatively low luminosity. If this understanding proves correct, we could hardly apply the dust-formation modelling adopted in the previous cases so far discussed, given the poor knowledge of the mass-loss mechanism characterizing the transition to the post-AGB phase during and after the star experiences a late TP. We speculate that the large IR excess observed in the SED of J052220.98 is caused by a fast removal of the residual envelope, which favoured large mass-loss rates, with enhanced dust production.

6.5. Oxygen-rich, faint post-AGB stars

We consider J050221.17 as representative of low-mass stars that failed to reach the C-star stage. As discussed in Sect. 4.2, this source descends from a low-mass progenitor, whose mass at the beginning of the AGB phase was around 0.8 $M_{\odot}$. Results from stellar evolution modelling indicate that such low-mass stars with the same metallicity as J050221.17 experience between four and five thermal pulses before their external envelope, initially of mass ~0.3 $M_{\odot}$, is lost, and the contraction to the post-AGB phase starts. The surface chemistry is substantially unchanged since the beginning of AGB evolution. Similarly to the carbon stars discussed earlier, the largest rates of mass loss, which in this particular case are of the order of 10^{-6} $M_{\odot}$ yr^{-1}, are reached at the tip of the AGB.

The dust formed in the wind of these stars is mainly composed by silicates, with alumina dust contributing for less than 10% (Dell'Agli et al. 2014a). Following the method described in Sect. 2, we find that the optical depth at the tip of AGB is $\tau_{10} = 0.5$.

We modelled dust formation in the wind for different points taken along the evolutionary track, following the same criterion, based on the values of the effective temperature, chosen for carbon stars: in this specific case, considering that the tip effective temperature is ~3600 K, we considered $T_{\rm eff} = 4000, 4500, 5000$ K. In analogy with the study of carbon stars presented earlier in this section, we used the radii of the star during each of the phases considered, in combination with the distance of the dust layer, derived for J050221.17 in Sect. 3, namely $R_{\rm in} = 5.45 \times 10^4\, R_{\odot}$, to calculate the current optical depth via Eq. (4). The results are shown in Fig. 13, where we report the values of τ_{10}^{now} as a function of the effective temperature.

The expected duration of the evolution of the star between the tip of the AGB and nowadays is ~60 000 yr. Given the the current distance of the dusty region from the central star $R_{\rm in}$, this implies that the dust particles have moved extremely slowly since they were released, with average velocities below 0.1 km s^{-1}. This is main reason why we believe it is extremely unlikely that the

dust responsible for the IR excess currently observed was released while the star was evolving at the tip of AGB. A further motivation for disregarding this possibility is that the derived $\tau_{10}^{\rm now}$ is significantly higher than that derived in Sect. 3.

Indeed the results shown in Fig. 13 indicate that consistency between the expected and the derived τ_{10} are found under the hypothesis that the dust was released when the effective temperature was in the 4000−4500 K range. In the latter case, we should assume that the time elapsed since the dust was released is substantially shorter, which would correspond to average velocities $\sim$0.5−1 km s^{-1}. These velocities are lower than those found during the study of the wind of carbon stars, which, according to our understanding, is the reason why in the case of M-type post-AGB stars the distance between the dusty cloud and the central object is smaller than for C-rich stars, as is clear in the right panel of Fig. 9. The generally lower extinction coefficients of silicates with respect to carbonaceous dust species is the main reason for the lower expansion velocity with which the dust moved away from O-rich stars than for the C-rich counterparts. Furthermore, M-type stars are the faintest objects in the sample studied here, and thus the effects of the radiation pressure on the dust particles, which is proportional to the luminosity of the star, are lower.

6.6. An overall view of dust surrounding post-AGB stars

The results presented in this section allow us to interpret the findings reported in Fig. 9. The increasing trend of the optical depth with luminosity (and thus mass) traced by metal-poor carbon stars is mainly due to the fact that brighter stars evolve faster during the AGB-post-AGB transition, and thus the dusty region is closer to the stellar surface. The higher carbon dust-production rates of the stars of higher mass also plays a role in this context.

Oxygen-rich stars that failed to reach the C-star stage cover a narrower range of luminosities than the C-rich counterparts, and thus no significant trends can be detected. The dust-production rate during the late evolutionary phases is significantly smaller than for carbon stars, and thus the acceleration experienced by the outflow is lower, and the current distances of the dusty regions from the photosphere are shorter.

The SEDs of carbon-rich post-AGB stars with sub-solar chemistry ($Z \sim 0.004$) present smaller IR excesses with respect to the lower-metallicity counterparts. This is due to the scarcity of gaseous carbon molecules available to form dust, which are in turn related to the large surface oxygen abundances.

7. Conclusions

We studied a sample of single stars identified as post-AGB sources observed in the Magellanic Clouds, with the goal of providing a characterization in terms of mass and formation epoch of the progenitors, and of the mineralogy of the dust responsible for the observed IR excess. The analysis is based on the combination of optical and near-IR data, which allowed us to trace the morphology of the spectral energy distribution.

The comparison between the observations and synthetic SED modelling obtained via the radiative transfer code DUSTY allowed us to identify a majority of stars surrounded by carbonaceous dust, and five objects with silicates in the surroundings. The determination of the luminosity, still obtained within the SED fitting process, led to the derivation of the initial mass of the progenitors, based on the tight link between core mass and luminosity that characterize post-AGB stars. Overall, we find that the sub-sample selected is composed of stars descending from progenitors with masses in the 0.7−2.5 $M_{\odot}$ range, formed in epochs ranging from 500 Myr to 8 Gyr ago.

For some of the stars considered, the interpretation proposed here finds a valid confirmation based on the results from high-resolution spectroscopy, which nicely agree with the expectations from stellar evolution modelling. The only exception is a star with luminosity $\sim$4500 $L_{\odot}$, inconsistent with the presence of carbon dust in the surroundings, for which we propose an alternative explanation, based on the occurrence of a late thermal pulse. Overall, the present analysis indicates that the results from the present generation of AGB models are consistent with the post-AGB observations, as far as the general pattern of the surface chemistry with luminosity is concerned. This agreement demands further investigation before it can be confirmed, given the small number of sources investigated.

The analysis of the IR excess observed, combined with results from evolutionary modelling of the late-AGB and post-AGB phases, proves a valuable tool in order to understand the physical behaviour of the stars before and during the AGB-post-AGB transition, as well as to study the dynamics of the outflow, moving away from the central stars dust currently observed was released.

The general conclusion drawn in this context is that the dust observed nowadays around post-AGB stars was released after contraction to the post-AGB phase began, and the effective temperatures increased to $\sim$4000 K. The IR excess observed is primarily determined by the timescale of post-AGB evolution, which proves crucial to determine the current location of the dusty region, and the dust-production rate experienced when the stars evolve through the tip of the AGB and the early post-AGB phase.

In the case of carbon stars, the IR excess increases with the luminosity of the stars, as bright stars evolve faster and are expected to experience a more efficient formation of dust. Detailed comparison with stellar evolution modelling indicates that the mass-loss and dust-formation rates of $M \geq 2\,M_{\odot}$ stars are correctly described, whereas in the low-mass domain, an increase of a factor of roughly is required. A further indication from the present study, connected with the small IR excess characterizing the SED of a few low-mass stars of sub-solar chemical composition, is the need for a mass-loss prescription that is sensitive to the surface chemistry, particularly to the carbon excess with respect to oxygen.

The oxygen-rich stars in the sample are interpreted as the progeny of low-mass stars that failed to reach the C-star stage. The dust in their surroundings is mostly composed of silicates in a crystalline form. In this case, a satisfactory agreement is found with the theoretical expectations, which indicate mass-loss rates at the tip of the AGB of the order of $10^{-6}\,M_{\odot}\,{\rm yr}^{-1}$. The dusty shells of M-type stars are found to be, on average, closer to the central star with respect to carbon stars, which we interpret as a result of the lower radiation pressure acting on silicates than on carbon dust, which results in slower winds.

As a next step in our research, we intend to extend our study to the Galactic sample of post-AGB stars presented in Kamath et al. (2022). The upcoming release of the *Gaia* DR3 astrometric data will be instrumental in further capitalising on the Galactic sample of objects. Additionally, in a future work, we will aim to obtain robust observational evidence to further constrain the dust chemical composition of our target sample. In this regard, high-resolution IR and mid-IR spectra from the JWST, covering the $\sim$5–28 μm wavelength regime, will be particularly useful since the spectra of post-AGB stars show interesting features, such as atomic fine-structure and hydrogen

lines, PAHs, crystalline and amorphous silicates, SiC, MgS, the enigmatic 21 μm feature, alumina, C_2H_2, SiS, SiO, TiO, and H_2O (Sloan et al. 2016; Gielen et al. 2011). The intermingling of these observations with our newly developed models will allow us to further develop our description of dust formation in the outflows from post-AGB stars.

Acknowledgements. D.K. acknowledges the support of the Australian Research Council (ARC) Discovery Early Career Research Award (DECRA) grant (DE190100813). This research was supported in part by the Australian Research Council Centre of Excellence for All Sky Astrophysics in 3 Dimensions (ASTRO 3D), through project number CE170100013. H.V.W. acknowledges support from the Research Council of the KU Leuven under grant number C14/17/082. E.M. acknowledges support from the INAF research project "LBT – Supporto Arizona Italia".

References

Blöcker, T. 1995, A&A, 297, 727
Blöcker, T. 2001, Ap&SS, 275, 1
Canuto, V. M. C., & Mazzitelli, I. 1991, ApJ, 370, 295
Castelli, F., & Kurucz, R. L. 2003, Modell. Stellar Atmos., 210, A20
Cloutman, L. D., & Eoll, J. G. 1976, ApJ, 206, 548
Dell'Agli, F. 2012, Master Thesis, University of Rome "Roma Tre", Italy
Dell'Agli, F., García-Hernández, D. A., Rossi, C., et al. 2014a, MNRAS, 441, 1115
Dell'Agli, F., Ventura, P., Garcia, Hernandez D., A., , et al. 2014b, MNRAS, 442, L38
Dell'Agli, F., Ventura, P., Schneider, R., et al. 2015a, MNRAS, 447, 2992
Dell'Agli, F., García-Hernández, D. A., Ventura, P., et al. 2015b, MNRAS, 454, 4235
Dell'Agli, F., Di Criscienzo, M., Boyer, M. L., et al. 2016, MNRAS, 460, 4230
Dell'Agli, F., Di Criscienzo, M., Ventura, P., et al. 2018, MNRAS, 479, 5035
Dell'Agli, F., Di Criscienzo, M., García-Hernández, D. A., et al. 2019, MNRAS, 482, 4733
Dell'Agli, F., Marini, E., D'Antona, F., et al. 2021, MNRAS, 502, L35
De Smedt, K., Van Winckel, H., Kamath, D., et al. 2015, A&A, 583, A56
Ferrarotti, A. S., & Gail, H.-P. 2006, A&A, 447, 553
Freytag, B., Ludwig, H.-G., & Steffen, M. 1996, A&A, 313, 497
Gielen, C., Cami, J., Bouwman, J., et al. 2011, A&A, 536, A54
He, J. H., Szczerba, R., Hasegawa, T. I., & Schmidt, M. R. 2014, ApJS, 210, 26
Herwig, F. 2000, A&A, 360, 952
Iben, I., & Renzini, A. 1983, ARA&A, 21, 271
Iben, I., Kaler, J. B., Truran, J. W., et al. 1983, ApJ, 264, 605
Jaeger, C., Mutschke, H., Begemann, B., Dorschner, J., & Henning, Th 1994, A&A, 292, 641
Jones, O. C., Kemper, F., Srinivasan, S., et al. 2014, MNRAS, 440, 631
Kamath, D., Wood, P. R., & Van Winckel, H. 2014, MNRAS, 439, 2211
Kamath, D., Wood, P. R., & Van Winckel, H. 2015, MNRAS, 454, 1468
Kamath, D., Dell'Agli, F., Ventura, P., et al. 2021, MNRAS, submitted, ArXiv e-prints [arXiv:2112.05535]
Kamath, D., Van Winckel, H., Ventura, P., et al. 2022, ApJ, 927, L13
Klochkova, V. G., Panchuk, V. E., & Tavolzhanskaya, N. S. 2015, AstL, 41, 14
Marigo, P. 2002, A&A, 387, 507
Marini, E., Dell'Agli, F., Di Criscienzo, M., et al. 2020, MNRAS, 493, 2996
Marini, E., Dell'Agli, F., Groenewegen, M. A. T., et al. 2021, A&A, 647, A69
Nanni, A., Bressan, A., Marigo, P., et al. 2013, MNRAS, 434, 2390
Nanni, A., Bressan, A., Marigo, P., et al. 2014, MNRAS, 438, 2328
Nenkova, M., Ivezic, Z., & Elitzur, M. 1999, Thermal Emission Spectroscopy and Analysis of Dust, Disks, andRegoliths, 20
Ossenkopf, V., Henning, Th., & Mathis, J. S. M. 1992, A&A, 261, 567
Pegourie, B. 1988, A&A, 194, 335
Sackmann, I.-J., & Boothroyd, A. I. 1992, ApJ, 392, L71
Sloan, G. C., Kraemer, K. E., McDonald, I., et al. 2016, ApJ, 826, 44
Sylvester, R. J., Kemper, F., Barlow, M. J., et al. 1999, A&A, 352, 587
van Aarle, E., Van Winckel, H., De Smedt, K., et al. 2013, A&A, 554, A106
van Hoof, P. A. M., Oudmaijer, R. D., & Waters, L. B. F. M. 1997, MNRAS, 289, 371
Ventura, P., Zeppieri, A., Mazzitelli, I., & D'Antona, F. 1998, A&A, 334, 953
Ventura, P., Di Criscienzo, M., Schneider, R., et al. 2012, MNRAS, 420, 1442
Ventura, P., Di Criscienzo, M., Carini, R., & D'Antona, F. 2013, MNRAS, 431, 3642
Ventura, P., Dell'Agli, F., Schneider, R., et al. 2014, MNRAS, 439, 977
Ventura, P., Karakas, A. I., Dell'Agli, F., et al. 2015, MNRAS, 450, 3181
Volk, K., Hrivnak, B. J., Matsuura, M., et al. 2011, ApJ, 735, 127
Wachter, A., Schröder, K. P., Winters, J. M., Arndt, T. U., & Sedlmayr, E. 2002, A&A, 384, 452
Wachter, A., Winters, J. M., Schröder, K. P., & Sedlmayr, E. 2008, A&A, 486, 497
Woods, P. M., Oliveira, J. M., Kemper, F., et al. 2011, MNRAS, 411, 1597
Zubko, V. G., Mennella, V., Colangeli, L., et al. 1996, MNRAS, 282, 132